nature portfolio

https://doi.org/10.1038/s41929-021-00618-w

Supplementary information

Analysis of the limitations in the oxygen reduction activity of transition metal oxide surfaces

In the format provided by the authors and unedited

Supplementary Information

Analysis of the Limitations in the Oxygen Reduction Activity of Transition Metal Oxide Surfaces

Hao Li[1,§], Sara Kelly[2,§], Dan Guevarra[3], Zhenbin Wang[1], Yu Wang[3], Joel A. Haber[3], Megha Anand[1], G.T. Kasun Kalhara Gunasooriya[1], Christina Susan Abraham[1], Sudarshan Vijay[1], John M. Gregoire[3], and Jens K. Nørskov[1,*]

[1] Catalysis Theory Center, Department of Physics, Technical University of Denmark, 2800 Lyngby, Denmark

[2] Department of Chemical Engineering, Stanford University, Stanford, CA 94305, USA

[3] Joint Center for Artificial Photosynthesis, Division of Engineering and Applied Science, California Institute of Technology, Pasadena, CA 91125, USA

[§] These authors contributed equally to this work.

***Corresponding Author:**

jkno@dtu.dk (J.K.N.);

Supplementary Discussion

High-throughput experiments

While the automation of the serial electrochemistry enables such unprecedented catalyst screening campaigns, several artifacts can occur, prompting our development of automated quality control measures to mitigate their influence of the characterization of catalyst activity. Intermittent electrochemical contact, typically from a bubble blocking contact to any 1 of the 3 electrodes, as well as oscillations or undesirably large working electrode contact area from electrolyte flow deregulation, cause erroneous measurements. Quality control requirements include (i) measured potential must be within 5 mV of intended potential for all but 25 data points acquired during a given technique, (ii) given the consistency of the shapes of CVs, PCA reconstruction of each CV using 9 components, which explained 99% of the variance in the entire dataset, was compared to the measured CV with a requirement of root mean squared difference of no more than 0.01 mA/cm^2, which removes CVs with anomalous shapes due to intermittent cell issues, and (iii) exploiting prior knowledge that catalytic activity is smooth on the scale of 10 at.% within a given composition space, each measured current density was required to be within 2 σ of the composition-smoothed value, where the predicted value and uncertainty were determined by training a Matern Gaussian process regressor ($\nu = 1.5$, $\alpha = 0.01$, and length_scale = 10 at.%) on the other compositions in the composition space. Measurements and associated current densities meeting these requirements are tabulated in the tables in https://data.caltech.edu/records/1632, which include both the full sample list including duplicate compositions as well as the set of catalyst activities after de-duplication using the median

current density for duplicate compositions. This latter table is the source for all data in **Figure 1** and **Supplementary Figures 1** and **3**. Note that these high-throughput TMO samples are expected to have a mixture of different Miller facets since many stable facets (with both low- and higher-index) of complex TMOs appear to have similar calculated surface energies. Therefore, the overall ORR activity of each sample should consist of the activity contribution from various surfaces and sites.

Importantly, the Pt baseline comparisons in **Figure 1** and **Supplementary Figure 1** (from Ref.[1]) used geometric surface area with smooth films whose microscopic surface area was confirmed to be similar *via* CO-stripping experiments. For the non-Pt catalysts in high-throughput experiments, interpretation of surface area measurements such as CO stripping are not standard. For TMO catalysts deposited with similar elements, loading, and thermal processing, we previously characterized electrochemical surface area *via* the electrochemical capacitance, finding that the specific surface area ratio can be up to a factor of 10.[2] As a result, while **Figure 1** and **Supplementary Figure 1** make comparisons on a geometric surface area basis, the analogous comparison on a microscopic surface area basis would result in the Pt baseline remaining approximately the same value while the TMO current densities being lowered by up to a factor of 10, further highlighting the inability of the TMOs to approach the activity of Pt.

Supplementary Methods

Statistical analysis on previous literature

Data for the statistical analysis of the TMOs for acidic ORR were acquired from the representative literatures published over the past twelve years (**Figure 1** and **Supplementary**

Figures 1-2).[3–32] These literatures include pure TMOs, oxynitride, oxycarbide, and oxidized carbonitride (CNO) TMOs. For comparison, the corresponding values of pure Pt were acquired from Ref.[1]. Note that the literatures with potential Pt-contamination and the partially oxidized Pt-alloy systems (which possess metallic Pt as their active sites) are excluded from the statistics.

Computational methods

The density functional theory (DFT) calculated binding energy data consist of our calculations and the previously reported data from our group.[33–36] For the transition metal (111) surfaces (Pt, Pd, Au, Ag, Cu, Rh, Ir, and Ni), 4-layer, 4×4 slabs were considered for calculations. Spin-polarization was employed in the calculations for Ni(111). A (3×3×1) *k*-point mesh was used to sample the Brillouin zone of these transition metal surfaces using the Monkhorst-Pack method.[37] The atop-site adsorption of oxygen on transition metal surfaces were relaxed by constraining the x-y direction of O*, where the O* was originally placed at the center of the metal-atop position before structural relaxation. The E_{HO*} *vs* E_{O*} scaling relation for transition metals used for microkinetic modeling was calculated by picking the most favorable site for each adsorbate (the grey line in **Figure 3b**). The cations of the TMO structures considered in this study include Zr, Hf, Ti, Sn, Ir, Pt, Rh, Nb, Re, Mn, Fe, V, Ni, Co, Pb, Pd, Ru, Sb, Mo, Sr, and La. For the TMOs containing Mn, Fe, Co, Ni, or Mo, spin-polarized DFT+U method[38] was adopted with Hubbard U values in line with the *MaterialsProject*.[39] The electronic energy and structural relaxation were converged to 10^{-5} eV and 0.05 eV/Å, respectively. For the rest of the structures, spin-polarizations were tested and used when necessary. All of the bulk structures were obtained from the *MaterialsProject* database.[39] Bulk optimizations were performed for each system

before their surfaces were cut, with the lattice parameters fully relaxed with a *k*-point density of at least 100 $Å^{-3}$ (reciprocal lattice volume). For the ORR binding energy calculations, the bottom half layers were fixed to the bulk positions, and the rest layers were relaxed. A vacuum spacing of at least 12 Å was placed in the direction perpendicular to the surface. We used the same *k*-point mesh grid as the bulk but setting the *z*-direction to be one because of the large vacuum and slab thickness. For all of the computation parameters above, stricter criteria (*i.e.*, larger kinetic cutoff, larger *k*-point mesh grid, lower convergent force, thicker layer, and larger unit cell) were tested for each system; no significant difference was found in the binding energies and adsorption geometries. The crystal structure manipulation and input generation were performed using Python Materials Genomics (pymatgen)[40] and Atomic Simulation Environment (ASE)[41] packages. The electronic binding energy data classified by the type of host cation are shown in **Supplementary Figure 6**. The data with the HO binding energy higher than ~2 eV are excluded from our analysis. For the free energy diagram analysis shown in **Figure 2**, (111) was used as an example because it is one of the lowest energy facets of ZrO_2 and HfO_2.[42,43]

The electronic binding energies were calculated using the total energies of H_2 and H_2O as the energy references:

$$E_{O*} = E_{tot} - E_{bare} - E_{H_2O} + E_{H_2}, (1)$$

$$E_{HO*} = E_{tot} - E_{bare} - E_{H_2O} + \frac{1}{2}E_{H_2}, (2)$$

$$E_{HOO*} = E_{tot} - E_{bare} - 2E_{H_2O} + \frac{3}{2}E_{H_2}, (3)$$

where E_{tot} is the total energy of the surface with adsorbate, E_{bare} is the total energy of a bare surface, E_{H_2O} is the total energy of a H_2O molecule in vacuum, and E_{H_2} is the total energy of a

H_2 molecule in vacuum. For most of the TMO surfaces considered in our calculations, the metal-atop was found to be the adsorption site of ORR adsorbate. The reaction free energy diagrams on TMOs were calculated with the computational hydrogen electrode (CHE) method,[44] with the entropic, zero-point energy, and solvation corrections shown in Refs.[44,45]. The free energy data for Pt, Pd, and Au were acquired from Ref.[46]. Surface Pourbaix diagrams were developed to show the most favorable surface state of a TMO as a function of pH and U_{SHE}, based on the representation of the adsorption of possible hydrogenated and oxygenated species in ORR:

$$H_nO_m^* + (2m-n)(H^+ + e^-) \rightleftarrows * + mH_2O. \quad (4)$$

Then the free energies shown in the surface Pourbaix diagrams (G_{SP}) were calculated based on the method described by Refs.[47–49] and the entropic and zero-point energy corrections from Refs.[44,49]:

$$G_{SP} = G_{bare} + mG_{H_2O} - G_{tot} - (2m-n)(\frac{1}{2}G_{H_2} - U_{SHE} - 2.303k_BT * pH), \quad (5)$$

where m and n respectively represent the numbers of oxygen and hydrogen atoms adsorbed on a stoichiometric TMO surface, k_B is the Boltzmann constant, and T is the temperature.

The O*-induced charge density differences ($\Delta\rho$) were plotted using the following equation:

$$\Delta\rho = \rho_{tot} - \rho_{bare} - \rho_{O*}, \quad (6)$$

where ρ_{tot} is the charge density of the surface with the adsorbed O, ρ_{bare} is the charge density of the bare surface, and ρ_{O*} is the charge density of the atomic oxygen.

Kinetic modeling methods

The microkinetic modeling of ORR volcano was based on the method by Hansen *et al.*[50] and Kelly *et al.*[51] using the CatMAP package.[52] The adsorbate coverages were determined by the steady-state approximation method. The rates for intermediate steps were calculated using Equation 7:

$$\text{rate} = k_f \prod \theta_{reac} - k_r \prod \theta_{prod} \text{ , (7)}$$

where θ_{reac} and θ_{prod} are the coverages of reactants and products, respectively. The rate constant k was calculated as the function of reaction prefactor A (s^{-1}), activation free energy G_a, Boltzmann constant k_B, and reaction temperature T:

$$k = A\ Exp[-\frac{G_a}{k_B T}] \text{ , (8)}$$

The intermediate reactions considered in the modeling are shown in Reactions 9-16:

O_2 (aq) → O_2 (dl), (9)

O_2 (dl) + * → O_2*, (10)

O_2* + (H^++e^-) + * → HOO*, (11)

HOO* + (H^++e^-) → O* + H_2O(l) , (12)

O* + (H^++e^-) → HO*, (13)

HO* + (H^++e^-) → H_2O(l) + *, (14)

HOO* + (H^++e^-) → H_2O_2*, (15)

H_2O_2* → H_2O_2(aq) + *, (16)

Reaction 9 stands for the diffusion of aqueous O_2 *via* a Nernstian diffusion layer, with the rate of 8×10^5 s^{-1} according to the calculations by Hansen *et al*.[50] Reaction 10 represents the adsorption of O_2 on the surface. Reaction 16 represents the desorption of formed H_2O_2 on the surface. Prefactors of both Reactions 10 and 16 were set as 1×10^8 s^{-1} due to the solvent reorganization to accommodate O_2 and H_2O_2.[51] Reactions 11-15 are the proton-electron transfer steps, with the energy of proton-electron pair represented by the energy of half of a H_2 molecule according to the CHE method.[44] Reactions 11-14 represent the standard associative pathway for $4e^-$ ORR. Reactions 11 and 15 represent the $2e^-$ ORR process. For Reaction 12, where the O-O is broken along with the protonation, data from Ref.[34], where G_a were calculated for the backward reaction, were reformulated to find $G_a = 0.8(G_{o*} - G_{HOO*}) + 1.35 + 0.42U$. For all other proton-transfers, which did not include any other bond-breaks, we used an intrinsic barrier of 0.26 eV and assumed 0.5 electrons had transferred at the transition state.[53] Prefactors for all of the proton-electron transfer steps were set as 1×10^9 s^{-1} to account for solvent reorganization.[51] Previous studies with explicit solvation models have shown that many TMO surfaces are hydrophobic, with the water layer floating above the surface and further stabilizing the adsorption of HOO* and HO*.[45,53,54] Zenkin *et al*. proposed an empirical theory that TMOs with lower metal electronegativity (*e.g.*, Zr and Hf oxides) tend to be more hydrophobic,[55] in good agreement with many previous experimental measurements.[56–58] Since the most widely reported stable TMOs for acidic ORR have relatively low electronegativity (*e.g.*, Zr, Nb, and Hf oxides), we consider these as hydrophobic TMOs. With the adsorption of HO* or HOO* under reaction conditions, due to the formed hydrogen bond with the water layer, the hydrophobicity of a TMO surface will be reduced. But since this will further strengthen the binding of HO* and HOO*,[45]

water is still less likely to block the surface site. Therefore, H_2O molecule is not expected to block the surface sites in our modeling. We note that whether TMOs can be hydrophobic or hydrophilic also depends on surface chemistry, which is still an interesting open question in the field. Dissociation reactions have been shown to have little effect on kinetics of ORR, and were therefore ignored.[51] Scaling relations for O* and HOO* were input using the scaling relations as discussed in the maintext, with the entropic, zero-point energy, and solvation corrections shown in previous Refs.[44,45]. Scaling relations for all other adsorbates were obtained from Kelly *et al*.[51] Then they were corrected for the RHE scale and electric field using Equation 17:[51]

$$G_{ads} = G_{ads}^{\vec{E}=0} + \mu\vec{E} - \frac{\alpha}{2}\vec{E}^2 - neU_{RHE} \text{ , (17)}$$

where $G_{ads}^{\vec{E}=0}$ is the binding energy of an adsorbate calculated without external electric field.

Our recent study showed how electric field effects can predict pH effects in ORR catalysts.[51] This is because the electric field is dependent on the absolute potential of the electrode, which can be approximated with a parallel-plate capacitor model, as shown in Equation 18:

$$\vec{E} = \frac{C_H}{\epsilon\epsilon_0}(U - U_{PZC}), \text{ (18)}$$

where U_{PZC} refers to the potential of zero charge of an electrode. There is little to no data on the potential of zero charge of TMOs, meaning our model cannot predict rates at specific pH for a given U_{RHE}. However, because U_{RHE} differs from potential *vs* the standard hydrogen electrode (U_{SHE}, and absolute potential scale) by only pH, as shown in Equation 19, we can generally predict that higher pH leads to more negative fields, and vice versa.

$$U_{SHE} = U_{RHE} - k_B T \ln(10) \times pH, \text{ (19)}$$

The values of μ and α were acquired from the second order polynomial fitting for the energy of each adsorbate across the range of electric fields, using Equation 17 where $\vec{E}$ is the applied electric field in the calculations using the Quantum Espresso package.[59] The volcano modeling for metal used the field effects calculations on Au(100) as described previously.[51] For the modeling of TMO volcanos, electric field effect calculations on ZrO_2(111) and ZrO_2(100) were considered for higher and low-index TMOs, respectively, with the reason that ZrO_2 is one of the most typical TMOs for acidic ORR and it behaves similar to other widely studied early TMOs.[5] Our electric field effect calculations on other TMOs indicate that the tuning trends of ORR adsorbate bindings are general (**Supplementary Figure 7**), which do not qualitatively alter with different types of TMO surfaces and in turn will not change the qualitative trends of the kinetic volcano. Since a more realistic solvation configuration on TMOs is with the water layer floating above the TMO surfaces due to the hydrophobic nature of many stable ORR TMOs (*e.g.*, Zr, Nb, and Hf oxides, as discussed earlier), the possibility of water blocking the reaction sites is not considered. Calculations with more explicit water molecules were performed with applied fields; no significant change was found in the overall configurations. Our recent study showed that this modeling method leads to excellent agreement with the pH-dependent trends of polarization curves and rotating ring disk electrode current experiments for Pt(111), Au(111), and Au(100).[51] Therefore, given the neglectable change in the water layer configuration with applied field, and the high consistency between our modeling results and experiments, field effect is not expected to qualitatively influence the reaction mechanism. Besides, though water molecules may bind differently to TMOs and to metals, we did not consider an aqueous electrolyte in the present study due to the current good agreement between theory and experiments, and the tremendous

computational cost for liquid-surface interface simulations. In addition, aqueous and double-layer oxygen were set to the energy of 5.19 eV at 0 V without external electric field. The mole fraction of oxygen was set as 2.34×10^{-5}, which corresponds to 1 atm O_2 in equilibrium with water.[51] To more clearly see the effects of each possible rate-determining step, we also included rate-determining step analysis. We used rates solved previously to describe the left and right hand side of the metal volcano and also calculated the rate of Reaction 12 using steady-state assumption (**Supplementary Figure 8**).

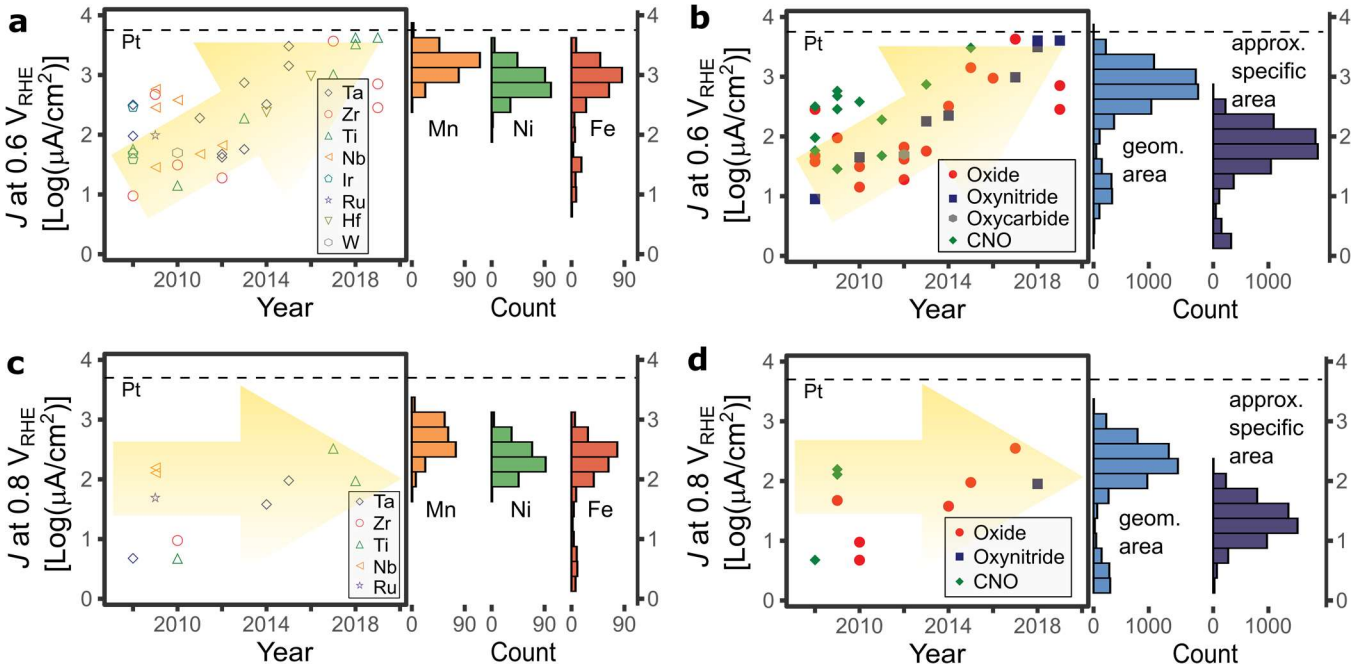

Supplementary Figure 1. Summary of the performance of TMO catalysts for ORR. In each subfigure, literature values published over the last twelve years for acidic ORR are shown in a scatter plot and the high-throughput alkaline ORR screening from the present work is shown as histograms. Current densities measured at the potential of 0.6 V_{RHE} (or 0.63 V_{RHE}) are shown labelled by cation system in a) and by host anion in b). Current densities measured at the potential of 0.8 V_{RHE} are shown labelled by cation system in c) and by host anion in d). For the catalyst compositions synthesized with more than 50% Mn, Ni, or Fe, the geometric current density histograms for each element are shown in a) and c). For the high-throughput screening results, the full dataset of TMOs is shown in b) and d), by geometric current density on the left (blue) and then by specific current density assuming an approximate specific surface area ratio of 10 (purple). The dashed lines are the values of pure Pt catalysts for acidic ORR reported by Ref.[1]. Catalysts with current density below 1 $\mu A/cm^2$ are not shown.

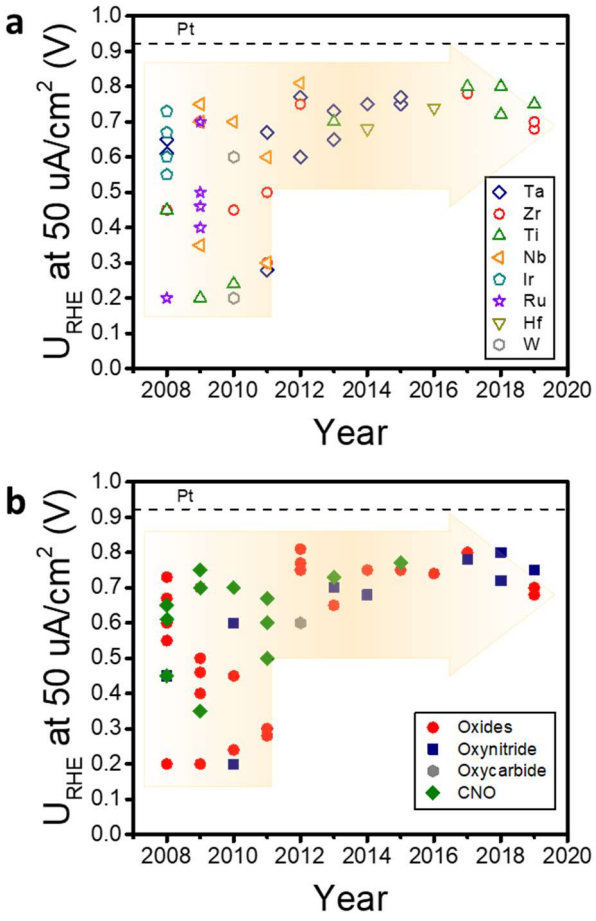

Supplementary Figure 2. Summary of the performance of TMO catalysts for acidic ORR published over the last twelve years. U_{RHE} measured at 50 μA/cm^2 with the data sorted by a) cation system and b) host anion. The dashed line is the value of pure Pt catalysts for acidic ORR reported by Ref.[1]. Note that the literatures with potential Pt-contamination and the partially oxidized Pt-alloy systems (which possess metallic Pt as their active sites) are excluded from the statistics.

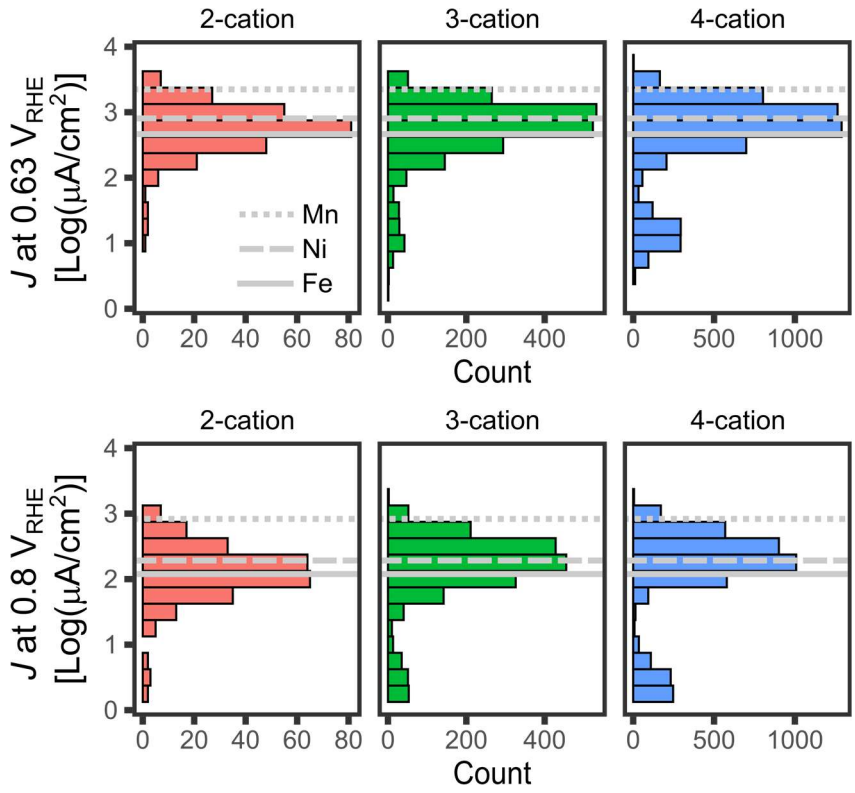

Supplementary Figure 3. Summary of high-throughput screening of 7798 unique TMO compositions. The values for the Mn, Ni, and Fe oxide samples are indicated by horizontal lines. The activity of the catalysts containing 2, 3, and 4 cations are shown in the respective histograms for 0.63 (top) and 0.8 (bottom) V_{RHE}. Catalysts with current density below 1 $\mu A/cm^2$ are not shown.

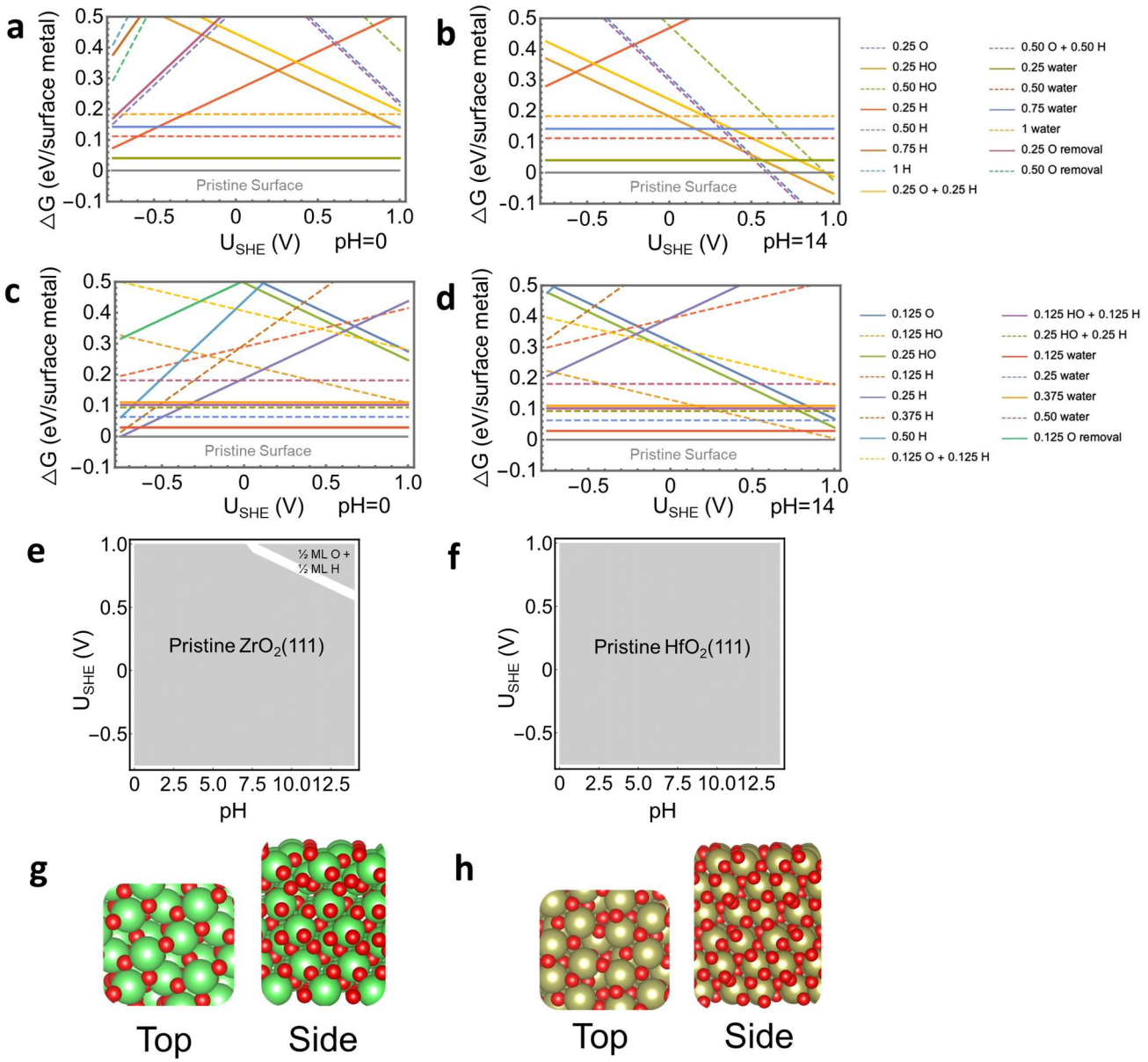

Supplementary Figure 4. Calculated surface Pourbaix diagrams for ZrO_2 and HfO_2(111). a-b) Surface Pourbaix diagrams of ZrO_2(111) at the pH of 0 and 14. c-d) Surface Pourbaix diagrams of HfO_2(111) at the pH of 0 and 14. e-f) 2D surface Pourbaix diagram of ZrO_2 and HfO_2(111). At U_{RHE}=0.80 V, the corresponding U_{SHE} values are 0.8 and -0.03 V respectively for the pH of 0 and 14. g-h) Top and side view of the pristine surfaces of ZrO_2 and HfO_2(111) considered for calculations. Red, green, and brown spheres represent O, Zr, and Hf atoms, respectively.

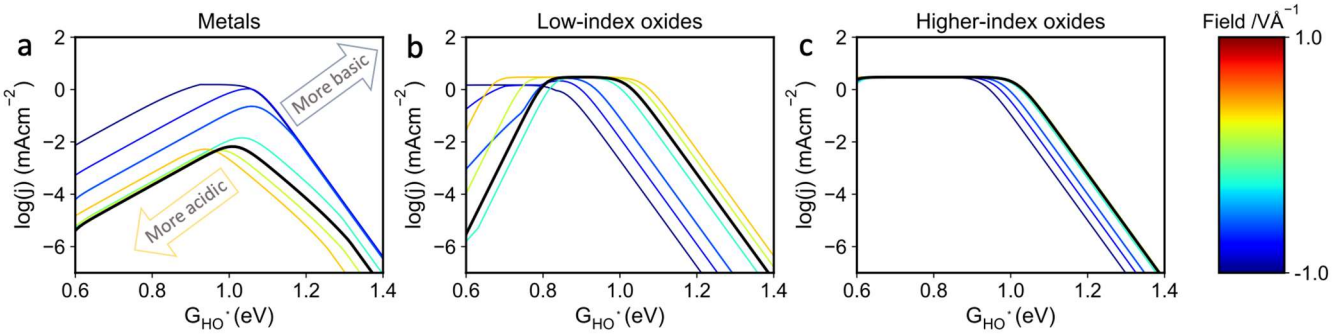

Supplementary Figure 5. pH-dependent kinetic volcano models for the 2e$^-$ ORR process at 0.6 V_{RHE}. a) Volcano activity models for transition metal surfaces; b,c) volcano activity models for b) low- and c) higher-index TMO surfaces. The higher and lower electric fields respectively represent more acidic and basic conditions.

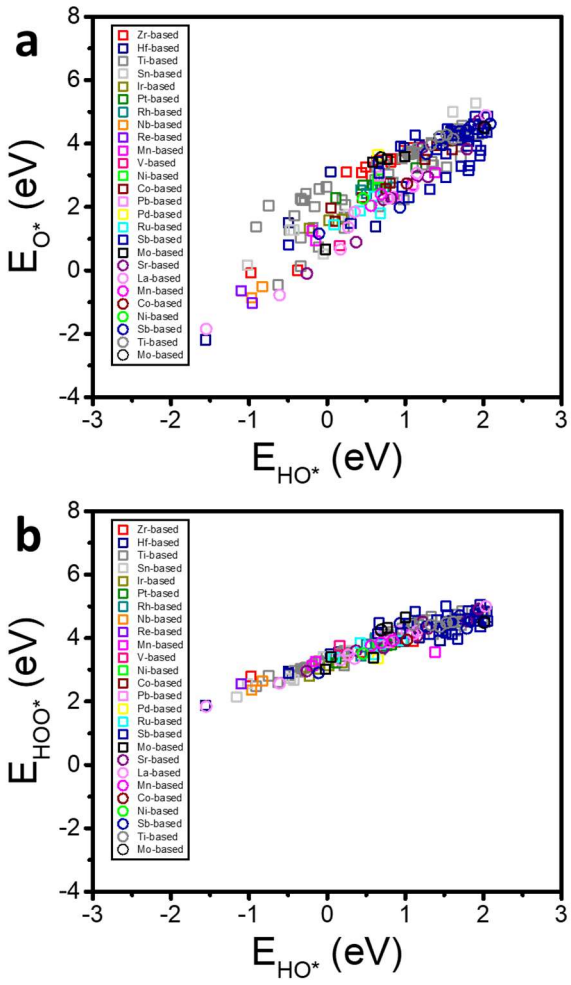

Supplementary Figure 6. ORR adsorbate binding energy data used in this study. a) E_{HO*} *vs* E_{O*} and b) E_{HO*} *vs* E_{HOO*} scaling relations. Square and circle points represent higher-($h^2+k^2+l^2 >1$) and low-index ($h^2+k^2+l^2 =1$) surfaces, respectively. The plots consist of the data from Refs.[33–36], and the data calculated by our current research team.

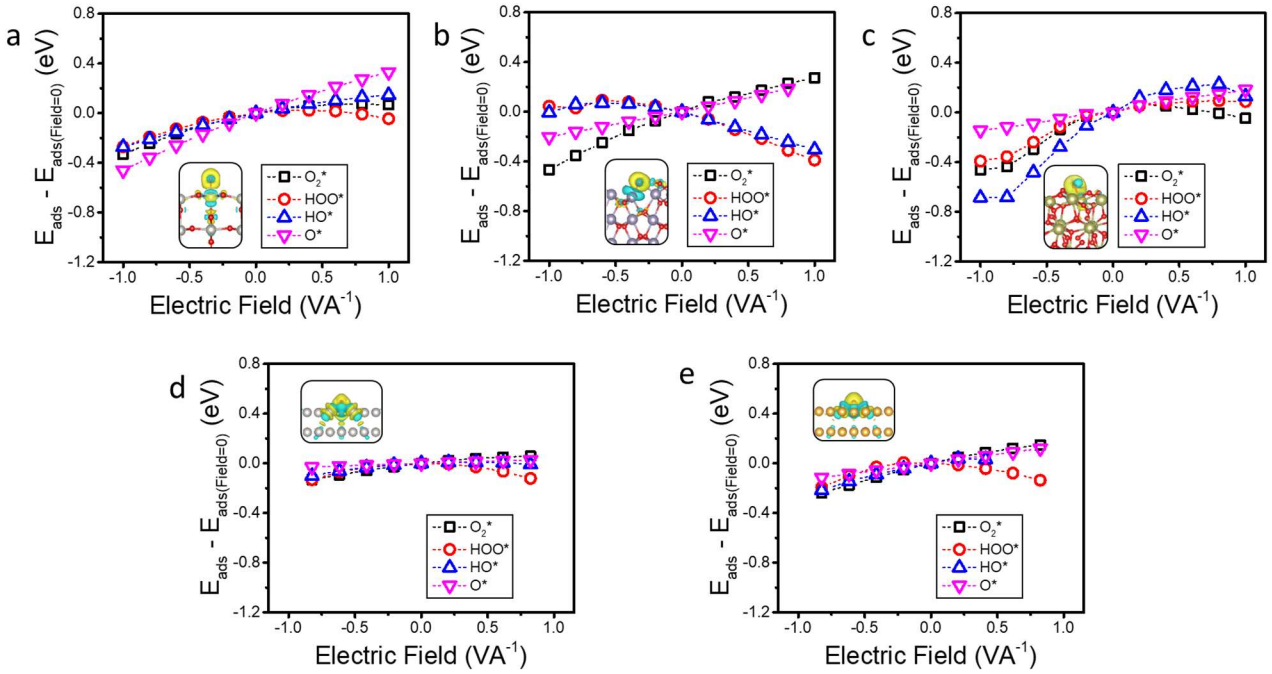

Supplementary Figure 7. Electric field effects on the ORR adsorbate bindings. a) PdO_2(110), b) SnO_2(110), c) HfO_2(111), d) Pt(111),[51] and e) Au(111).[51] Insets show the charge density differences induced by the adsorption of atomic oxygen. The yellow and teal colors in the isosurfaces represent electron charge gain and loss, respectively. Red, sliver, purple, brown, grey, and yellow spheres represent O, Pd, Sn, Hf, Pt, and Au, respectively.

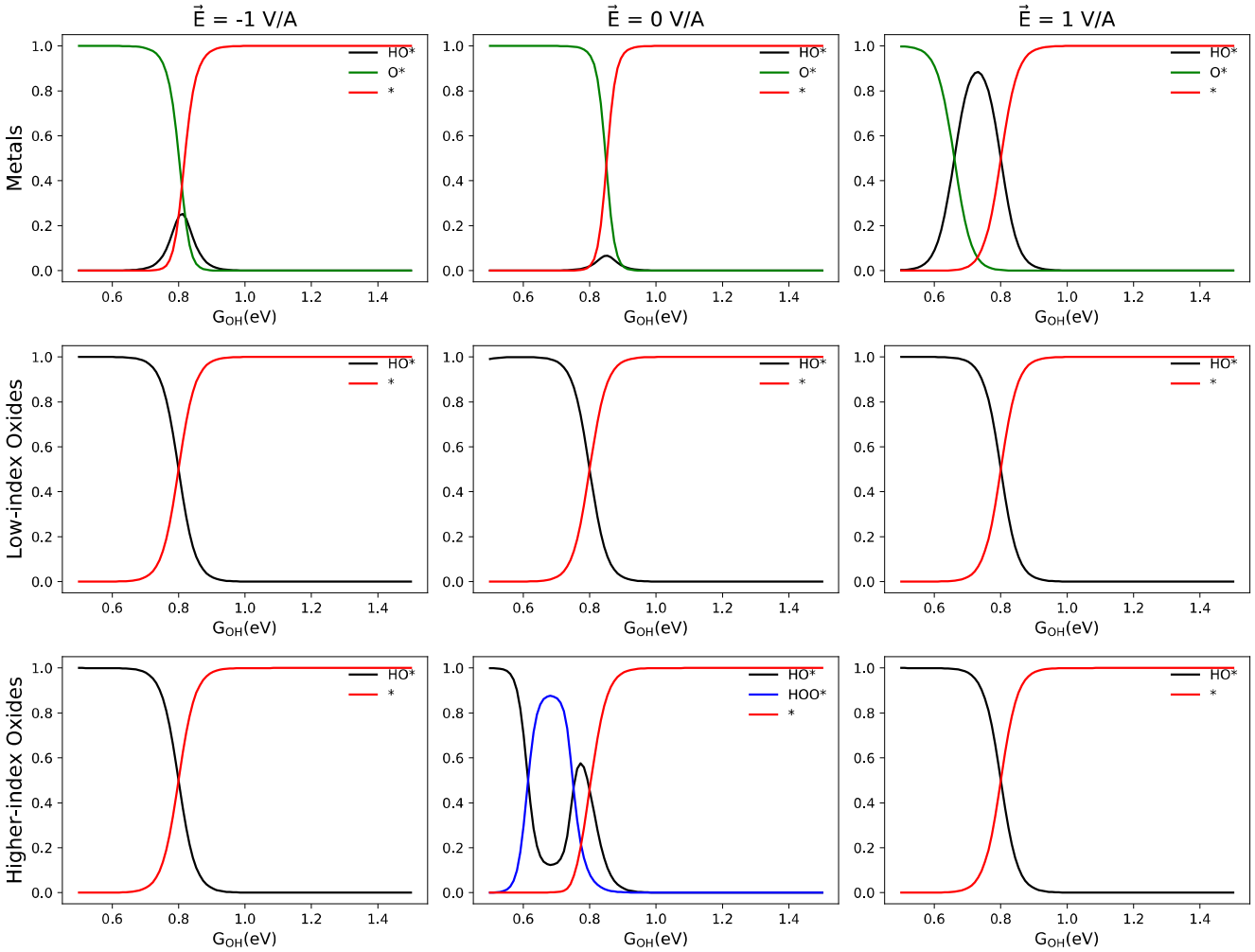

Supplementary Figure 8. Simulated steady-state coverages of ORR adsorbates. Fractional coverages of each adsorbate with at least 1% coverage of surface sites across the binding energy range. Coverages shown for metals, low-index TMOs, and higher-index TMOs at -1, 0, and 1 V/Å fields.

Supplementary References

1. Escudero-Escribano, M. *et al.* Tuning the activity of Pt alloy electrocatalysts by means of the lanthanide contraction. *Science (80-.).* **352**, 73–76 (2016).
2. Haber, J. A. *et al.* Discovering Ce-rich oxygen evolution catalysts, from high throughput screening to water electrolysis. *Energy Environ. Sci.* **7**, 682–688 (2014).
3. Ishihara, A. *et al.* Tantalum oxynitride for a novel cathode of PEFC. *Electrochem. Solid-State Lett.* **8**, A201 (2005).
4. Ishihara, A., Shibata, Y., Mitsushima, S. & Ota, K. Partially Oxidized Tantalum Carbonitrides as a New Nonplatinum Cathode for PEFC–1–. *J. Electrochem. Soc.* **155**, B400–B406 (2008).
5. Seo, J., Cha, D., Takanabe, K., Kubota, J. & Domen, K. Electrodeposited ultrafine NbOx, ZrOx, and TaO x nanoparticles on carbon black supports for oxygen reduction electrocatalysts in acidic media. *ACS Catal.* **3**, 2181–2189 (2013).
6. Maekawa, Y., Ishihara, A., Kim, J. H., Mitsushima, S. & Ota, K. I. Catalytic activity of zirconium oxynitride prepared by reactive sputtering for ORR in sulfuric acid. *Electrochem. Solid-State Lett.* **11**, B109–B112 (2008).
7. Liu, Y., Ishihara, A., Mitsushima, S. & Ota, K. ichiro. Influence of sputtering power on oxygen reduction reaction activity of zirconium oxides prepared by radio frequency reactive sputtering. *Electrochim. Acta* **55**, 1239–1244 (2010).
8. Lee, N. W. *et al.* Highly Conductive Off-Stoichiometric Zirconium Oxide Nanofibers with Controllable Crystalline Structures and Bandgaps and Improved Electrochemical

Activities. *ACS Appl. Energy Mater.* **2**, 3513–3522 (2019).

9. Chisaka, M. *et al.* Zirconium Oxynitride-Catalyzed Oxygen Reduction Reaction at Polymer Electrolyte Fuel Cell Cathodes. *ACS Omega* **2**, 678–684 (2017).
10. Madkikar, P. *et al.* Nanometric Fe-Substituted ZrO2 on Carbon Black as PGM-Free ORR Catalyst for PEMFCs. *J. Electrochem. Soc.* **166**, F3032–F3043 (2019).
11. Takasu, Y., Suzuki, M., Yang, H., Ohashi, T. & Sugimoto, W. Oxygen reduction characteristics of several valve metal oxide electrodes in HClO4 solution. *Electrochim. Acta* **55**, 8220–8229 (2010).
12. Chisaka, M. & Morioka, H. Phosphor and nitrogen co-doped rutile TiO2 covered on TiN for oxygen reduction reaction in acidic media. *Catal. Sci. Technol.* **9**, 611–619 (2019).
13. Li, X., Liu, C., Xing, W. & Lu, T. Development of durable carbon black/titanium dioxide supported macrocycle catalysts for oxygen reduction reaction. *J. Power Sources* **193**, 470–476 (2009).
14. Chisaka, M. Creation of oxygen reduction reaction active sites on titanium oxynitride without increasing the nitrogen doping level. *Phys. Chem. Chem. Phys.* **20**, 15613–15617 (2018).
15. Ohgi, Y., Ishihara, A., Shibata, Y., Mitsushima, S. & Ota, K. I. Catalytic activity of partially oxidized transition-metal carbide-nitride for oxygen reduction reaction in sulfuric acid. *Chem. Lett.* **37**, 608–609 (2008).
16. Chisaka, M., Yamamoto, Y., Itagaki, N. & Hattori, Y. Active Site Formation for Oxygen Reduction Reaction on Carbon-Support-Free Titanium Oxynitride with Boosted Activity in Acidic Media. *ACS Appl. Energy Mater.* **1**, 211–219 (2018).

17. Tominaka, S., Ishihara, A., Nagai, T. & Ota, K. I. Noncrystalline Titanium Oxide Catalysts for Electrochemical Oxygen Reduction Reactions. *ACS Omega* **2**, 5209–5214 (2017).

18. Chisaka, M., Ishihara, A., Ota, K. I. & Muramoto, H. Synthesis of carbon-supported titanium oxynitride nanoparticles as cathode catalyst for polymer electrolyte fuel cells. *Electrochim. Acta* **113**, 735–740 (2013).

19. Nam, K. D. *et al.* Partially oxidized niobium carbonitride as a non-platinum catalyst for the reduction of oxygen in acidic medium. *Electrochim. Acta* **55**, 7290–7297 (2010).

20. Takasu, Y., Yoshinaga, N. & Sugimoto, W. Oxygen reduction behavior of RuO2/Ti, IrO2/Ti and IrM (M: Ru, Mo, W, V) Ox/Ti binary oxide electrodes in a sulfuric acid solution. *Electrochem. commun.* **10**, 668–672 (2008).

21. Takasu, Y., Oohori, K., Yoshinaga, N. & Sugimoto, W. An examination of the oxygen reduction reaction on RuO2-based oxide coatings formed on titanium substrates. *Catal. Today* **146**, 248–252 (2009).

22. Chisaka, M., Sasaki, H. & Muramoto, H. Monoclinic hafnium oxynitride supported on reduced graphene oxide to catalyse the oxygen reduction reaction in acidic media. *Phys. Chem. Chem. Phys.* **16**, 20415–20419 (2014).

23. Chisaka, M. & Itagaki, N. Evaluation and Enhancement of the Oxygen Reduction Reaction Activity on Hafnium Oxide Nanoparticles Assisted by L(+)-lysine. *Electrochim. Acta* **201**, 279–285 (2016).

24. Ando, T., Izhar, S., Tominaga, H. & Nagai, M. Ammonia-treated carbon-supported cobalt tungsten as fuel cell cathode catalyst. *Electrochim. Acta* **201**, 279–285 (2010).

25. Ishihara, A. *et al.* Synthesis of nano-TaOx oxygen reduction reaction catalysts on multi-walled carbon nanotubes connected via a decomposition of oxy-tantalum phthalocyanine. *Phys. Chem. Chem. Phys.* **17**, 7643–7647 (2015).

26. Nam, K. D., Ishihara, A., Matsuzawa, K., Mitsushima, S. & Ota, K. I. Partially oxidized niobium carbonitride as non-platinum cathode for PEFC. *Electrochem. Solid-State Lett.* **12**, B158 (2009).

27. Seo, J. *et al.* Highly dispersed TaOx nanoparticles prepared by electrodeposition as oxygen reduction electrocatalysts for polymer electrolyte fuel cells. *J. Phys. Chem. C* **117**, 11635–11646 (2013).

28. Seo, J., Cha, D., Takanabe, K., Kubota, J. & Domen, K. Particle size dependence on oxygen reduction reaction activity of electrodeposited TaOx catalysts in acidic media. *Phys. Chem. Chem. Phys.* **16**, 895–898 (2014).

29. Uehara, N. *et al.* Tantalum oxide-based electrocatalysts made from oxy-tantalum phthalocyanines as non-platinum cathodes for polymer electrolyte fuel cells. *Electrochim. Acta* **179**, 146–153 (2015).

30. Ota, K. I. *et al.* Development of group 4 and 5 metal oxide-based cathodes for polymer electrolyte fuel cell. *J. Power Sources* **196**, 5256–5263 (2011).

31. Ishihara, A. *et al.* Emergence of oxygen reduction activity in partially oxidized tantalum carbonitrides: Roles of deposited carbon for oxygen-reduction-reaction-site creation and surface electron conduction. *J. Phys. Chem. C* **177**, 18837–18844 (2013).

32. Ohgi, Y. *et al.* Oxygen reduction reaction on tantalum oxide-based catalysts prepared from TaC and TaN. *Electrochim. Acta* **68**, 192–197 (2012).

33. Man, I. C. *et al.* Universality in Oxygen Evolution Electrocatalysis on Oxide Surfaces. *ChemCatChem* **3**, 1159–1165 (2011).

34. Dickens, C. F., Kirk, C. & Nørskov, J. K. Insights into the electrochemical oxygen evolution reaction with ab initio calculations and microkinetic modeling: Beyond the limiting potential volcano. *J. Phys. Chem. C* **123**, 18960–18977 (2019).

35. García-Mota, M. *et al.* Tailoring the activity for oxygen evolution electrocatalysis on rutile TiO2(110) by transition-metal substitution. *ChemCatChem* **3**, 1607–1611 (2011).

36. Bajdich, M., García-Mota, M., Vojvodic, A., Nørskov, J. K. & Bell, A. T. Theoretical investigation of the activity of cobalt oxides for the electrochemical oxidation of water. *J. Am. Chem. Soc.* **135**, 13521–13530 (2013).

37. Monkhorst, H. & Pack, J. Special points for Brillouin zone integrations. *Phys. Rev. B* **13**, 5188–5192 (1976).

38. Dudarev, S. & Botton, G. Electron-energy-loss spectra and the structural stability of nickel oxide: An LSDA+U study. *Phys. Rev. B - Condens. Matter Mater. Phys.* **57**, 1505–1509 (1998).

39. Jain, A. *et al.* Commentary: The materials project: A materials genome approach to accelerating materials innovation. *APL Mater.* **1**, 011002 (2013).

40. Ong, S. P. *et al.* Python Materials Genomics (pymatgen): A robust, open-source python library for materials analysis. *Comput. Mater. Sci.* **68**, 314–319 (2013).

41. Marcin, A. H. L. and J. J. M. and J. B. and I. E. C. and R. C. and *et al.* The atomic simulation environment—a Python library for working with atoms. *J. Phys. Condens. Matter* **29**, 273002 (2017).

42. Mukhopadhyay, A. B., Sanz, J. F. & Musgrave, C. B. First-principles calculations of structural and electronic properties of monoclinic hafnia surfaces. *Phys. Rev. B - Condens. Matter Mater. Phys.* **73**, 115330 (2006).

43. Christensen, A. & Carter, E. A. First-principles study of the surfaces of zirconia. *Phys. Rev. B - Condens. Matter Mater. Phys.* **58**, 8050 (1998).

44. Nørskov, J. K. *et al.* Origin of the overpotential for oxygen reduction at a fuel-cell cathode. *J. Phys. Chem. B* **108**, 17886–17892 (2004).

45. Gauthier, J. A., Dickens, C. F., Chen, L. D., Doyle, A. D. & Nørskov, J. K. Solvation Effects for Oxygen Evolution Reaction Catalysis on IrO2(110). *J. Phys. Chem. C* **121**, 11455–11463 (2017).

46. Kulkarni, A., Siahrostami, S., Patel, A. & Nørskov, J. K. Understanding Catalytic Activity Trends in the Oxygen Reduction Reaction. *Chem. Rev.* **118**, 2302–2312 (2018).

47. Hansen, H. A., Rossmeisl, J. & Nørskov, J. K. Surface Pourbaix diagrams and oxygen reduction activity of Pt, Ag and Ni(111) surfaces studied by DFT. *Phys. Chem. Chem. Phys.* **10**, 3722–3730 (2008).

48. Vinogradova, O., Krishnamurthy, D., Pande, V. & Viswanathan, V. Quantifying Confidence in DFT-Predicted Surface Pourbaix Diagrams of Transition-Metal Electrode-Electrolyte Interfaces. *Langmuir* **34**, 12259–12269 (2018).

49. Valdés, Á., Qu, Z. W., Kroes, G. J., Rossmeisl, J. & Nørskov, J. K. Oxidation and photo-oxidation of water on TiO2 surface. *J. Phys. Chem. C* **112**, 9872–9879 (2008).

50. Hansen, H. A., Viswanathan, V. & Nørskov, J. K. Unifying kinetic and thermodynamic analysis of 2 e- and 4 e- reduction of oxygen on metal surfaces. *J. Phys. Chem. C* **118**,

6706–6718 (2014).

51. Kelly, S. R., Kirk, C., Chan, K. & Nørskov, J. K. Electric Field Effects in Oxygen Reduction Kinetics: Rationalizing pH Dependence at the Pt(111), Au(111), and Au(100) Electrodes. *J. Phys. Chem. C* **124**, 14581–14591 (2020).

52. Medford, A. J. *et al.* CatMAP: A Software Package for Descriptor-Based Microkinetic Mapping of Catalytic Trends. *Catal. Letters* **145**, 794–807 (2015).

53. Tripkovic, V. & Vegge, T. Potential- and Rate-Determining Step for Oxygen Reduction on Pt(111). *J. Phys. Chem. C* **121**, 26785–26793 (2017).

54. Rossmeisl, J., Qu, Z. W., Zhu, H., Kroes, G. J. & Nørskov, J. K. Electrolysis of water on oxide surfaces. *J. Electroanal. Chem.* **607**, 83–89 (2007).

55. Zenkin, S. *et al.* Thickness dependent wetting properties and surface free energy of HfO2 thin films. *Appl. Phys. Lett.* **108**, 231602 (2016).

56. Lin, S. S. & Liao, C. S. Effects of the ratio of O2/Ar pressure on wettability and optical properties of HfO2 films before and after doping with Al. *Appl. Surf. Sci.* **380**, 229–236 (2016).

57. Sarkar, S. & Pradhan, S. K. Tailoring of optical and wetting properties of sputter deposited silica thin films by glancing angle deposition. *Appl. Surf. Sci.* **209**, 509–513 (2014).

58. Zenkin, S., Kos, Š. & Musil, J. Hydrophobicity of Thin Films of Compounds of Low-Electronegativity Metals. *J. Am. Ceram. Soc.* **97**, 2713–2717 (2014).

59. Giannozzi, P. *et al.* QUANTUM ESPRESSO: A modular and open-source software project for quantum simulations of materials. *J. Phys. Condens. Matter* **21**, 395502 (2009).